Crystal growth, low-temperature spectroscopy and multi-watt laser operation of Yb:$Ca_3NbGa_3Si_2O_{14}$

Xuzhao Zhang[1,2], Pavel Loiko[3], Xavier Mateos[1,*], Josep Maria Serres[1], Junyu Ren[2], Jiayi Guo[2], Rui Cheng[2], Cunyuan Gao[2], Qing Dong[2], Venkatesan Jambunathan[4], Antonio Lucianetti[4], Tomas Mocek[4], Elena Vilejshikova[5], Uwe Griebner[6], Valentin Petrov[6], Zhengping Wang[2,**], Shiyi Guo[2,***], Xinguang Xu[2,] Magdalena Aguilo[1], and Francesc Diaz[1]

[1]*Física i Cristal·lografia de Materials i Nanomaterials (FiCMA-FiCNA)-EMaS, Dept. Química Física i Inòrganica, Universitat Rovira i Virgili (URV), Campus Sescelades, E-43007 Tarragona, Spain*
[2]*State Key Laboratory of Crystal Materials and Institute of Crystal Materials, Shandong University, 250100 Jinan, China*
[3]*ITMO University, 49 Kronverkskiy pr., 197101 St. Petersburg, Russia*
[4]*HiLASE Centre, Institute of Physics CAS, Za Radnicí 828, 25241 Dolní Břežany, Czech Republic*
[5]*Center for Optical Materials and Technologies (COMT), Belarusian National Technical University, 65/17 Nezavisimosti Ave., 220013 Minsk, Belarus*
[6]*Max Born Institute for Nonlinear Optics and Short Pulse Spectroscopy, Max-Born-Str. 2a, D-12489 Berlin, Germany*

**Corresponding author: xavier.mateos@urv.cat*
***e-mail: zpwang@sdu.edu.cn*
****e-mail: syguo@sdu.edu.cn*

Abstract We report on the crystal growth, structure, room- and low-temperature (6 K) absorption and emission spectroscopy of a 3 at.% Yb^{3+}-doped trigonal ordered langasite-type silicate crystal, $Ca_3NbGa_3Si_2O_{14}$ (Yb:CNGS). The Rietveld refinement data are presented. Absorption, stimulated-emission and gain cross-sections are determined for the Yb^{3+} ion in CNGS for π and σ polarizations. The maximum stimulated emission cross-section amounts to $\sigma_{SE} = 0.97\times10^{-20}$ cm^{-2} at 1014 nm (σ-polarization). The Stark splitting of the Yb^{3+} multiplets is resolved. Microchip laser operation is obtained with both *a*-cut and *c*-cut 3 at.% Yb:CNGS samples under end-pumping at 976 nm by a Volume Bragg Grating-stabilized diode laser. For the latter cut, the maximum output power reaches 7.61 W at 1048-1060 nm with a slope efficiency of 59%. By varying the output coupling, multi-watt emission over a 50 nm-broad spectral range is achieved.

Keywords: silicate crystals; ytterbium; crystal growth; spectroscopy; Stark splitting; stimulated emission.

1. Introduction

Langasite (lanthanum gallium silicate), $La_3Ga_5SiO_{14}$ (shortly LGS), has been known as a piezoelectric crystal since the 1980s [1-4], used for the fabrication of substrates of wide band bulk acoustic waves and surface acoustic waves filters [5,6]. LGS is a non-centrosymmetric trigonal crystal (point gr. 32, sp. gr. P321) [7]. It shows no phase transition up to its melting point at 1470 °C and can be grown by the conventional Czochralski (Cz) method [3,4,7]. LGS crystals doped with rare-earth ions (RE^{3+}) such as Nd^{3+}, Tm^{3+} and Eu^{3+} have been studied in terms of their spectroscopic properties [8-10]. Laser operation of Nd^{3+} in LGS crystals has been demonstrated in the continuous-wave (CW), passively Q-switched (PQS) and mode-locked (ML) operation regimes [11-13].

LGS belongs to a wide class of crystals with a general formula $A_3BC_3D_2O_{14}$ showing 4 types of cation sites [14]. The A and B cations are located in dodecahedral (distorted Thompson cubes) and octahedral sites, respectively, and the C and D ones – in tetrahedral sites. For langasite, La^{3+} occupies the A-sites, Ga^{3+} - B, C and half of the D sites. The Si^{4+} ions occupy the remaining half of the D-sites, representing a disordered crystal structure. Calcium niobium gallium silicate $Ca_3NbGa_3Si_2O_{14}$ (shortly CNGS) is another representative of the $A_3BC_3D_2O_{14}$ family [15] in which the Ca^{2+} ions are located in the A-sites, the Nb^{5+} ions in the B-sites and the Ga^{3+} and Si^{4+} ions in the C and D tetrahedral sites, respectively. CNGS is an ordered crystal. It can also be grown from the melt by the Cz method [15,16]. CNGS exhibits better mechanical, elastic and thermal properties than LGS and provides better transmission in the visible and near-IR [15-18].

Despite the modest thermal conductivity of CNGS (1.8 W/mK), it exhibits high specific heat (0.83 J/gK), weak and almost isotropic thermal expansion (~5.6×10^{-6} K^{-1}), and attractive elastic properties leading to high stress fracture limit [19]. Thus, these crystals are also attractive as laser crystals for power scaling when doped with RE^{3+} ions which replace the Ca^{2+} ones in the A-sites with an VIII-fold O^{2-} coordination [19]. The structure, elastic and spectroscopic properties of Nd^{3+}-doped CNGS were described in [18,20,21]. A CW diode-end-pumped Nd:CNGS laser was reported in [20] delivering 1.63 W at 1065 nm with a slope efficiency η of 31%. A ML Nd^{3+}:CNGS laser generating 759 fs pulses at a repetition rate of 43 MHz was also demonstrated [22]. Moreover, as CNGS is a non-centrosymmetric crystal, it is suitable for self-frequency-doubling, SFD, resulting in the development of green lasers [23].

The Yb^{3+} ion is more suitable than the Nd^{3+} ion for power scaling at ~1 μm as it features a simple energy-level scheme leading to high Stokes efficiency ($\eta_{St} = \lambda_p/\lambda_L$) and weak heat loading ($\eta_h \approx 1 - \eta_{St}$), as well as lack of parasitic processes, e.g. energy-transfer upconversion. The longer upper laser level lifetime of the Yb^{3+} ion is beneficial for PQS lasers and the broader spectral bands are advantageous for ML lasers. Recently, the growth, thermal properties and preliminary spectroscopic and laser characterization of a 5 at.% Yb:CNGS crystal were presented [19]. The laser output in the CW mode amounted to 1.53 W at 1060 nm with η = 48% [19]. SFD output was observed from type I and type II Yb:CNGS crystals [19]. Subsequently, we demonstrated the possibility of power scaling of diode-end-pumped compact Yb:CNGS lasers to the multi-watt level [24] and also proved that optimization of the

doping concentration between 1 and 5 at.% Yb is crucial to ensure simultaneously high pump efficiency and low intrinsic losses.

In the this work, we present details on the crystal growth by the Cz method, a detailed room- and low-temperature spectroscopic study and efficient and power-scalable CW micro-chip laser operation at ~1 μm of a 3 at.% Yb:CNGS crystal exploiting the two principal orientations along the *a* and *c* crystallographic axes.

2. Experimental

2.1 Crystal growth

CNGS melts congruently at ~1350 °C. In the present work, the Yb:CNGS crystal was grown by the conventional Czochralski (Cz) method. The polycrystalline mixtures were obtained by solid state reaction of 4N-pure $CaCO_3$, Nb_2O_5, Yb_2O_3, SiO_2 and 5N-pure Ga_2O_3 powders taken in stoichiometric proportion. The Yb^{3+} content was 3 at.% (with respect to Ca^{2+}). The powders were thoroughly mixed and pressed into cylindrical tablets. To ensure that the compounds react completely, the tablets were kept at 1150 °C for 24 h in a corundum crucible in air. After a slow cooling of the obtained polycrystalline tablets to room temperature (RT, 20 °C), they were put into an Ir crucible (diameter: 69 mm, height: 39 mm). As a seed, we used an undoped CNGS crystal oriented along the [100] crystallographic axis. It was fixed on a Pt holder. The Ir crucible with the growth charge was kept slightly above the melting point for 2-3 h to homogenize the charge before the growth process. The seed was rotated at 10-15 r.p.m. and the pulling rate was 0.3-1.0 mm/h. A multistep cooling method was used to avoid thermal shocks. The cooling rate increased from 10 to 40 °C/h. The total growth duration was ~82 h. The growth was performed in a mixture N_2 + 3 vol% O_2 atmosphere in order to reduce the number of oxygen vacancies. After the growth, the crystal boule was removed from the melt and cooled down slowly (at a rate of 50 °C/h) to RT. No annealing of the as-grown crystal was performed.

The as-grown boule of 3 at.% Yb:CNGS with dimensions of 23×25×43 mm^3 is shown in Fig. 1(a). It was crack- and inclusion-free and showed a slight yellowish coloration. The latter is related to color centers in the crystal due to the presence of O_2 in the growth atmosphere. A weak band centered at ~460 nm was observed in the absorption spectrum supporting this hypothesis. The cross-section of the cylindrical part of the boule was uniform over its length. The side surface featured a well-developed (001) face. From the bottom part of the as-grown boule, samples oriented along the [100] and [001] axes (*a*-cut and *c*-cut, respectively) were cut. Their cross-section was 3×3 mm^2 and the thickness was 4 mm. Both 3×3 mm^2 faces of the samples were polished to laser-grade quality, Fig. 1(b).

2.2 Characterization

The X-ray powder diffraction (XRD) pattern was measured using a Siemens D5000 diffractometer (Bragg-Brentano parafocusing geometry and vertical θ-θ goniometer) fitted with a curved graphite diffracted-beam monochromator, incident and diffracted beam Soller slits with a 0.06º receiving slit and a scintillation counter as a detector. The 2θ range was between 10º and 70º. The data were collected with an angular step of 0.05º at 3 s per step and sample

rotation. The Cu K_α radiation (1.54184 Å) was used. The refinement of the Yb:CNGS structure was performed by the Rietveld method using HighScore Plus software. A pseudo-Voigt function was selected to describe the line profiles. The structure parameters and atomic coordinates of undoped CNGS [25] were used as a starting model for the iteration procedure. The total number of parameters refined N was 44. The goodness of fit χ^2 was 3.72.

The Yb^{3+}:CNGS crystal is trigonal and, thus, optically uniaxial. Its optical axis is parallel to the c-axis. The absorption spectra for light polarizations π ($E \parallel c$) and σ ($E \perp c$) were measured using an a-cut sample with a Varian CARY-5000 spectrophotometer at RT and at low-temperature (LT, 6 K). In the latter case, we used an Oxford Instruments Ltd. cryostat (model SU 12) with helium-gas close-cycle flow. The spectral resolution was 0.08 nm.

To measure the emission spectra in polarized light (π and σ), we used a YOKOGAWA optical spectrum analyzer (OSA), model AQ 6373, and a Glan-Taylor polarizer. The spectral resolution was 0.1 nm. The spectra were recorded at 6 K, 50 K, 100 K, 200 K and at RT using the same cryostat. The luminescence was collected from the sample edge at 90° to the excitation beam to avoid the reabsorption effect. An InGaAs laser diode emitting at ~972 nm was used as an excitation source.

2.3 Laser set-up

The laser experiments were performed in a compact plano-plano (microchip type) cavity, Fig. 2. The uncoated crystal was mounted in a Cu-holder providing cooling from all lateral sides and Indium foil ensured a good thermal contact. The holder was water-cooled to 12 °C. The cavity consisted of a flat pump mirror (PM) antireflection (AR)-coated for 0.88-0.99 μm and high-reflection (HR)-coated for 1.01–1.23 μm, and a flat output coupler (OC) having a transmittance T_{OC} of 1%, 2.5%, 5%, 10%, 20% or 30 % for 1.02–1.2 μm. Both PM and OC were placed as close as possible to the polished crystal faces. The geometrical cavity length was then ~4 mm.

As pump source, we used a Volume Bragg Grating, (VBG)-stabilized InGaAs fiber-coupled diode laser (BWT Beijing LTD, fiber core diameter: 105 μm; numerical aperture N.A.: 0.22) emitting up to ~27 W at 975.8 nm (emission bandwidth: 0.7 nm). The unpolarized pump radiation (M^2 ~ 36) was collimated and focused into the crystal using a lens assembly (1:1 imaging ratio, focal length: 30 mm) resulting in a pump spot radius w_p of 52 μm and a Rayleigh length of $2z_R$ = 1.0 mm (in the crystal). All OCs provided partial reflection at the pump wavelength (~90%), so that the crystal was pumped in a double-pass. The total pump absorption under lasing conditions *Abs* was 60% and 58% for a-cut and c-cut crystals, respectively.

3. Results and discussion

4.1 Crystal structure

The measured XRD pattern of the 3 at.% Yb^{3+}:CNGS crystal is shown in Fig. 3. In the same figure, we also present the results of the Rietveld refinement showing good agreement with the measurement. The structure data are listed in Table 1. The 3 at.% Yb^{3+}:CNGS is trigonal (sp. gr. $P321$, No. 150, ICSD card #51-0178) and its lattice parameters are $a = b =$

8.0890(2) Å, c = 4.9815(1) Å, $\alpha = \beta = 90°$, $\gamma = 120°$ (number of formula units, Z = 1). The unit-cell volume is 282.30 Å^3 and the calculated density ρ_{calc} = 4.22 g/cm^3 which is slightly higher than the experimental value, ρ_{exp} = 4.16 g/cm^3, determined with the hydrostatic weighting method. The determined lattice parameters are close to those for undoped CNGS found in [16], a = 8.087 Å, c = 4.980 Å. In Table 2 and Table 3, we list the atomic coordinates (x, y, z) and the selected interatomic distances (Ca–O, Si–O, Nb–O, Ga–O and Ca–Ca) obtained after the Rietveld refinement.

In the Yb^{3+}:CNGS lattice, Fig. 4, the Ca^{2+}/Yb^{3+} ions are located in a twisted Thomson cube (A-site, 3*e* Wyckoff position, coordination number (C.N.) by O^{2-} is VIII) with relatively long Ca–O distances ranging from 2.33 to 2.82 Å. The Nb^{5+} ions are located in octahedrons (B-site, 1*a* Wyckoff position, C.N. = VI). The edge-sharing [CaO_8] and [NbO_6] polyhedrons form isolated planes parallel to the *a*-*b* plane. These planes are linked by [GaO_4] and [SiO_4] tetrahedrons (Wyckoff positions for Ga^{3+} and Si^{4+} ions: 3*f* and 2*d*, respectively, C.N. = IV). The Yb^{3+}:CNGS structure features relatively long Ca–Ca distances, 4.20-4.98 Å, which is favourable for Yb^{3+} doping because only weak concentration quenching of luminescence can be expected.

4.2 Optical spectroscopy

The RT absorption spectra of Yb^{3+}:CNGS are shown in Fig. 5(a). The absorption cross-sections, σ_{abs}, were calculated from the measured absorption coefficients α_{abs}, $\sigma_{abs} = \alpha_{abs}/N_{Yb}$ (the calculated N_{Yb} value was 3.2×10^{20} at/cm^3). The maximum σ_{abs} corresponds to σ-polarization, 1.25×10^{-20} cm^2 at 977 nm (0 → 0' transition, zero-phonon-line, ZPL, see below) and it is 1.4 times lower for π-polarization at the same wavelength. The feature of Yb^{3+}:CNGS is the clearly resolved double-peak absorption (977.0 and 979.1 nm) around the ZPL. The reason for the double-peak absorption will be explained below. The total full-width at half-maximum (FWHM) of the double-peak is 4.2 (π) and 4.6 (σ) nm, which makes Yb^{3+}:CNGS attractive for pumping with InGaAs laser diodes.

The LT (6 K) absorption spectra of Yb^{3+}:CNGS for π and σ polarizations are shown in Fig. 5(b). The double-peak structure is clearly preserved even at 6 K, with the energy of the two peaks being 10240 cm^{-1} (0 → 0', 976.6 nm) and 10210 cm^{-1} (979.3 nm). We attribute the second peak to the 1 → 0' transition from the first Stark sub-level "1" of the ground-state which is populated even at 6 K due to the low energy gap with the "0" sub-level (30 cm^{-1}). The peaks at 10645 and 10828 cm^{-1} are attributed to the 0 → 1' and 0 → 2' transitions, respectively. This assignment is in accordance with the Raman spectra of Yb^{3+}:CNGS [24]. As above mentioned, CNGS is an ordered crystal, thus, the two absorption peaks at 10240 and 10210 cm^{-1} cannot be assigned to ZPLs corresponding to two different crystallographic sites for Yb^{3+} ions. Indeed, the decay curve for a 1 at.% Yb:CNGS crystal presented in [24] was clearly single-exponential.

The polarized luminescence spectra of Yb^{3+}:CNGS at RT are shown in Fig. 6(a). They indicate strong anisotropy of the emission properties, with the higher emission intensity observed for σ-polarization. In the spectra, the double-peak feature around ZPL is clearly resolved with maxima at 977.0 and 979.1 nm, see inset in Fig. 6(a). In the long-wavelength re-

gion, where the laser operation is expected, three peaks centered at 1013, 1043 and 1063 nm are observed. For the most intense 1013 nm peak, the emission bandwidth (FWHM) is ~19 nm (σ) and 38 nm (π). The LT emission spectra are shown in Fig. 6(b). In addition to the above-mentioned double-peak corresponding to the 0' → 0 and 0' → 1 transitions, the peaks at 1011 and 1060 nm are due to the 0' → 2 and 0' → 3 transitions, respectively.

The LT absorption and emission spectroscopy allowed to determine the Stark splitting of the ground- and excited-states of the Yb^{3+} ion in CNGS, see Fig. 7(a). The total splitting of the $^2F_{7/2}$ multiplet is large, 806 cm^{-1}, and favorable for a quasi-three-level operation scheme. For the rare-earth, RE^{3+} ions, the barycenter of any $^{2S+1}L_J$ multiplet shows almost a linear variation vs. the barycenter of any isolated $4f^n$ multiplet, which is typically expressed as a barycenter plot [26]. For the Yb^{3+} ion, this rule is used to evaluate the assignment of the Stark sub-levels by plotting the barycenter of the $^2F_{5/2}$ multiplet vs. the barycenter of the $^2F_{7/2}$ one for various hosts [26,27], Fig. 7(b). Neglecting the *J*-mixing, the energy separation between the two barycenters should be constant and equal to the corresponding separation for the free Yb^{3+} ion (10167 cm^{-1}). The point corresponding to Yb^{3+}:CNGS is standing slightly out of the main dependence which is mostly due to the small energy separation between the 0 and 1 Stark sub-levels of the ground state. Such a deviation from the main trend is however possible for many crystals.

Stimulated-emission (SE) cross-sections σ_{SE} for the $^2F_{5/2} \rightarrow {}^2F_{7/2}$ transition of the Yb^{3+} ion in CNGS were calculated using two methods. The first one is based on the Füchtbauer–Ladenburg (F-L) equation [28]:

$$\sigma_{SE}^{i}(\lambda) = \frac{\lambda^5}{8\pi n_i^2 \tau_{Yb} c} \frac{3W_i(\lambda)}{\sum_{i=\pi,\sigma,\sigma} \int \lambda W_i(\lambda) \mathrm{d}\lambda}, \quad (1)$$

where $W_i(\lambda)$ is the measured luminescence spectrum for the *i*-th polarization (π or σ), λ is the wavelength, n_i is the refractive index (n_e = 1.85 and n_o = 1.77 at ~1 μm for π- and σ-polarization, respectively [20]), τ_{Yb} is the radiative lifetime of the emitting state ($^2F_{5/2}$), τ_{Yb} = 710 μs as measured from the fluorescence of 1 at.% Yb^{3+}:CNGS [24], *c* is the speed of light.

The second approach uses the reciprocity method (RM) [29]:

$$\sigma_{SE}^{i}(\lambda) = \sigma_{abs}^{i}(\lambda) \frac{Z_1}{Z_2} \exp\left(-\frac{hc/\lambda - E_{ZL}}{kT}\right), \quad (2)$$

where σ^i_{abs} is the absorption cross-section for the *i*-th polarization, *h* is the Planck constant, *k* is the Boltzmann constant, *T* is the crystal temperature (RT), E_{ZL} is the energy difference between the lowest Stark sub-levels of the two multiplets (ZPL, 10240 cm^{-1}), and Z_m are the partition functions of the lower (*m* = 1) and upper (*m* =2) manifolds:

$$Z_m = \sum_k g_k^m \exp(-E_k^m / kT). \quad (3)$$

Here, g^m_k (assumed to be 1) is the degeneration of the sub-level with the number *k* and energy E^m_k measured from the lowest sub-level of the multiplet, Fig. 7(a). For Yb^{3+} in CNGS, Z_1 = 2.056 and Z_2 = 1.192, so that Z_1/Z_2 = 1.725. The reciprocity method is useful to calculate the values of σ_{SE} in the spectral range where an overlap of absorption and emission bands occurs (the so-called reabsorption effect, strongly affecting the measured emission spectra), while

the F-L method is useful at the long-wavelength edge of the emission band where the reciprocity method can lead to a large error due to the exponential term in Eq. (2). To avoid this, we carefully measured the absorption spectra at 1025-1100 nm using the Varian CARY-5000 spectrophotometer with a long accumulation time and reduced spectral resolution of 0.5 nm.

The polarized σ_{SE} spectra for the Yb^{3+}:CNGS crystal at RT were calculated by both the F-L and reciprocity methods, see Fig. 8. They are in a reasonable agreement with each other. We attribute the residual deviation mostly to an imperfect calibration of the luminescence set-up for the measurements with polarized light. The maximum σ_{SE} for σ-polarization is 2.4×10^{-20} cm^2 at 977.0 nm (ZPL) while for π-polarization it is 1.5 times lower at the same wavelength. In the spectral range where laser operation is expected (at wavelengths longer than ZPL), an anisotropy of σ_{SE} is also observed: the maximum σ_{SE} values corresponding to a local peak at ~1014 nm are 0.97×10^{-20} cm^2 (σ) and 0.35×10^{-20} cm^2 (π). Here and above, the σ_{SE} values achieved with the reciprocity method are specified. Thus, for *a*-cut Yb^{3+}:CNGS, linear polarization of the laser output (σ) is expected. For *c*-cut Yb^{3+}:CNGS, unpolarized laser emission is expected while the stimulated-emission properties for this crystal cut will also correspond to σ-polarization.

The Yb^{3+} ion represents a quasi-three-level scheme exhibiting reabsorption and thus the gain cross-sections, $\sigma_g = \beta\sigma_{SE} - (1-\beta)\sigma_{abs}$, are typically calculated to predict the laser wavelength. Here, $\beta = N_2(^2F_{5/2})/N_{Yb}$ is the inversion ratio. The σ_g spectra for π or σ light polarizations and various inversion ratios β = 0.1...0.5 are shown in Fig. 9. For the calculation of the σ_g spectra, we used the σ_{SE} values calculated by means of the reciprocity method. For the laser polarization of interest (σ) and small $\beta < 0.1$, the gain cross-section spectrum is flat and broad, spanning from 1020 to 1080 nm. For larger β, a local peak centered at ~1014 nm is dominant in the σ_g spectra. For $\beta = 0.2$, the gain bandwidth amounts to ~43 nm (σ) and 48 nm (π). This indicates a potential of Yb^{3+}:CNGS for sub-100 fs mode-locked laser operation.

4.3 Laser operation

Microchip laser operation has been achieved with both *a*-cut and *c*-cut Yb^{3+}:CNGS crystals for all studied OCs (T_{OC} = 1%...30%). This indicates that both cuts provide a positive thermal lens [30]. For the *a*-cut crystal, the laser output was linearly polarized (σ), the polarization was naturally selected by the gain anisotropy, Fig. 9. No polarization-switching has been observed when changing the pump level. For the *c*-cut crystal, the laser emission was unpolarized. No damage of the crystals has been observed up to the maximum applied absorbed pump power, P_{abs} ~14 W.

The input-output dependences for the *a*-cut and *c*-cut 3 at.% Yb^{3+}:CNGS microchip lasers are shown in Fig. 10. For both cuts, the maximum laser output corresponded to T_{OC} = 2.5%. The *a*-cut Yb^{3+}:CNGS laser generated 7.29 W at 1048-1065 nm (multi-peak emission) with a slope efficiency η of 59% (with respect to P_{abs}). The laser threshold was at P_{th} = 0.60 W and the optical-to-optical efficiency η_{opt} reached 32% (with respect to the incident pump power). For the *c*-cut crystal, the maximum output power was slightly higher, 7.61 W at 1048-1060 nm with a similar η = 59% and a slightly lower P_{th} of 0.55 W. For higher OCs, the laser performance deteriorated whilst multi-watt output has been achieved with all of them.

This deterioration of the laser performance is attributed to the upconversion losses. The latter can arise from cooperative upconversion for Yb^{3+}-Yb^{3+} ion pairs and Tm^{3+} upconversion in an Yb^{3+}-Tm^{3+} system, as well as non-radiative energy transfer (ET) from excited Yb^{3+} ions to color centers present in the Yb:CNGS crystals. Tm^{3+} ions are frequently present as an impurity in the Yb_2O_3 reagent. As mentioned above, the Yb^{3+} ions represent a quasi-tree-level laser scheme. With the increase of the output coupling, the inversion (β) increases to compensate the losses. Larger β will naturally lead to higher probability of upconversion and ET processes. Indeed, with an increased T_{OC}, the intensity of the blue upconversion luminescence from Yb:CNGS crystals notably increased.

No thermal roll-over has been observed in the output dependences in Fig. 10. The only exception is in the case of T_{OC} = 1% for the *c*-cut crystal. This is because the [001] axis is perpendicular to the crystal growth direction (Fig. 1) and the optical quality of the *c*-cut crystal is slightly lower which is detrimental under a high intracavity power inherent for small T_{OC}.

The typical laser emission spectra for the *a*-cut and *c*-cut 3 at.% Yb^{3+}:CNGS microchip lasers are shown in Fig. 11. With the increase of T_{OC}, the laser wavelength experiences a blue-shift due to the quasi-three-level nature of the Yb^{3+} laser. For T_{OC} < 10%, multi-peak emission is observed due to the broad and smooth gain spectra of Yb^{3+}:CNGS for small inversion ratios (β < 0.1), Fig. 9(b), and due to the etalon effects arising from the air gaps between the PM, laser crystal and OC. For T_{OC} > 10%, the emission is around 1016 nm, corresponding to a local peak in the gain spectra for β > 0.1. By varying the output coupling, a multi-watt laser emission is observed with discrete lines in the spectral range of 1015-1065 nm (50 nm-broad, for the *a*-cut crystal).

We attribute the moderate slope efficiency of the Yb^{3+}:CNGS laser (as compared with the theoretical limit set by the Stokes efficiency, $\eta_{St} = \lambda_p/\lambda_L$ ~0.92 for 2.5% OC) to a non-optimum mode-matching (pump spot radius w_p = 52 μm) and the short Rayleigh length for the pump beam. The thermo-optical properties (dn/dT coefficients and thermal lensing) which are needed to calculate the size of the laser mode are not known for Yb^{3+}:CNGS crystals.

To qualitatively prove our hypothesis, we used another InGaAs diode laser with a 200 μm core diameter, N.A. of 0.22, emitting up to ~16 W at 977-981 nm (depending on the current) in the same set-up as in Fig. 2. This pump diode laser allows a better mode-matching with w_p = 100 μm and $2z_R$ = 1.8 mm. Due to the power dependent pump wavelength, the pump absorption in Yb^{3+}:CNGS varied from 22 to 43% (*a*-cut) and from 25 to 41% (*c*-cut). Microchip laser operation with both *a*-cut and *c*-cut Yb^{3+}:CNGS crystals was achieved using this second diode, see the summary of the output characteristics in Table 4. For the *a*-cut crystal and T_{OC} = 2.5%, the maximum output power was 3.28 W at ~1053 nm with η = 77%. The laser threshold was at P_{th} = 1.36 W (due to the larger pump spot size) and η_{opt} = 23%. For the *c*-cut crystal, even higher η = 83% was determined. Consequently, both power scaling and high slope efficiency are possible for compact Yb^{3+}:CNGS lasers.

In Table 5, we have compared the output characteristics of various crystals doped with Yb^{3+} ions and employed in diode-pumped solid-state lasers emitting at ~1 μm, according to recent publications [31-42].

4. Conclusion

Yb^{3+}-doped calcium niobium gallium silicate (Yb^{3+}:CNGS) is an attractive laser material. Large-volume crystals of 3 at.% Yb^{3+}:CNGS with high optical quality can be grown by the conventional Czochralski method providing access to various crystal orientations (*a*-cut and *c*-cut, as demonstrated in the present paper, and potentially to type I-cut for SFD). The Yb^{3+} ion in CNGS exhibits broad and intense spectral bands in polarized light which is a prerequisite for efficient diode-pumping and polarized laser output. Yb^{3+}:CNGS provides relatively large stimulated-emission cross-section, σ_{SE} = 0.97×10^{-20} cm^{-2} at 1014 nm (for σ-polarization), as determined using the RT and LT absorption and emission spectroscopy, and broad gain bandwidth (>40 nm). This makes this crystal attractive for broadly tunable CW and sub-100 fs ML lasers. Moreover, the long lifetime of the upper laser level of Yb^{3+}:CNGS (710 μs) is attractive for power-scalable PQS lasers. In the present work, using *a*-cut and *c*-cut 3 at.% Yb^{3+}:CNGS crystals in a compact microchip-type laser end-pumped by a VBG-stabilized diode laser at 976 nm, we have achieved > 7 W of CW output at ~1050 nm with a slope efficiency of 59%. By changing the output coupling, a discrete tuning of the laser emission in a 50 nm-broad range is demonstrated.

Acknowledgements

This work was supported by the Spanish Government (projects No. MAT2016-75716-C2-1-R, (AEI/FEDER,UE), MAT2013-47395-C4-4-R, TEC 2014-55948-R); Generalitat de Catalunya (2014SGR1358); National Natural Science Foundation of China (51472147, 61178060, 51672161). F.D. acknowledges additional support through the ICREA academia award 2010ICREA-02 for excellence in research. P.L. acknowledges financial support from the Government of the Russian Federation (Grant 074-U01) through ITMO Post-Doctoral Fellowship scheme. This work was co-financed by the European Regional Development Fund and the state budget of the Czech Republic (project HiLASE CoE: Grant No. CZ.02.1.01/0.0/0.0/15_006/ 0000674), by the European Union's Horizon 2020 research and innovation programme under grant agreement No. 739573, by the Ministry of Education, Youth and Sports of the Czech Republic (Programmes NPU I Project No. LO1602, and Large Research Infrastructure Project No. LM2015086).

References

1. A.B. Ilyaev, B.S. Umarov, L.A. Shabanova, M.F. Dubovik, Phys. Stat. Sol. (a) 98 (1986) K109-K114.
2. J. Stade, L. Bohatý, M. Hengst, R. B. Heimann, Cryst. Res. Technol. 37 (2002) 1113-1120.
3. K. Shimamura, H. Takeda, T. Kohno, T. Fukuda, J. Cryst. Growth 163 (1996) 388-392.
4. H. Kong, J. Wang, H. Zhang, X. Yin, S. Zhang, Y. Liu, X. Cheng, L. Gao, X. Hu, M. Jiang, J. Cryst. Growth 254 (2003) 360-367.
5. P. Zheng, T.L. Chin, D. Greve, I. Oppenheim, V. Malone, L. Cao, IEEE Trans. Ultrason., Ferroelect., Freq. Control 58 (2011) 1538-1540.
6. J.A. Thiele, M.P. Da Cunha, Sens. Actuators B: Chem. 113 (2006) 816-822.

7. G.M. Kuzmicheva, E.N. Domoroschina, V.B. Rybakov, A.B. Dubovsky, E.A. Tyunina, J. Cryst. Growth 275 (2005) 715-719.
8. A.A. Kaminskii, I.M. Silvestrova, S.E. Sarkisov, G.A. Denisenko, Phys. Stat. Sol. (a) 80 (1983) 607-620.
9. Y.S. Kim, K.H. Auh, Mater. Lett. 57 (2002) 28-31.
10. S. Georgescu, O. Toma, A.M. Chinie, L. Gheorghe, A. Achim, A.S. Stefan, Opt. Mater. 30 (2008) 1007-1012.
11. Q. Wang, Z. Wei, Y. Zhang, Z. Zhang, H. Yu, H. Zhang, Z. Wang, Opt. Lett. 36 (2011) 1770-1772.
12. J. Liu, Z. Wang, K. He, L. Wei, Z. Zhang, Z. Wei, J. Wang, Opt. Express 22 (2014) 26933-26938.
13. Y. Yu, J. Wang, H. Zhang, Z. Wang, H. Yu, M. Jiang, Opt. Lett. 34 (2009) 467-469.
14. B.V. Mill, E.L. Belokoneva, T. Fukuda, Russ. J. Inorg. Chem. 43 (1998) 1168–1175.
15. Z.M. Wang, X.F. Cheng, D.R. Yuan, L.H. Pan, S. Guo, D. Xu, M.K. Lv, J. Cryst. Growth 249 (2003) 240–244.
16. I.H. Jung, A. Yoshikawa, T. Fukuda, K.H. Auh, J. Alloys Compd. 339 (2002) 149-155.
17. S. Zhang, H. Kong, R. Xia, Y. Zheng, J. Xin, T.R. Shrout, Solid State Commun. 150 (2010) 435-438.
18. J. Ren, X. Zhang, X. Zhang, J. Guo, R. Cheng, S. Guo, Mater. Lett. 167 (2016) 122-124.
19. X. Zhang, Y. Zhou, J. Ren, D. Lu, H. Yu, Z. Wang, X. Xu, Cryst. Eng. Comm. 18 (2016) 5338-5343.
20. X. Zhang, X. Zhang, S. Guo, J. He, K. Han, F. Lou, X. Liu, Opt. Mater. Express 5 (2015) 977-985.
21. J. Ren, X. Zhang, X. Zhang, R. Cheng, J. Guo, X. Zhang, F. Yu, B. Huang, S. Guo, Cryst. Eng. Comm. 18 (2016) 3481-3487.
22. J. Li, X.-T. Zhang, J.-L. He, S. Guo, J. Ning, F. Lou, R. Zhao, X.-C. Su, J. Hou, B.-T. Zhang, Appl. Opt. 55 (2016) 5444-5448.
23. X. Zhang, Y. Zhou, A. Yasukevich, P. Loiko, X. Mateos, X. Xu, S. Guo, Z. Wang, Opt. Express 25 (2017) 19760-19766.
24. X. Zhang, P. Loiko, J.M. Serres, X. Mateos, J. Ren, Z. Wang, S. Guo, X. Xu, E. Vilejshikova, U. Griebner, V. Petrov, M. Aguiló, F. Díaz, Opt. Mater. Express 7 (2017) 3626-3633.
25. H. Ohsato, T. Iwataki, H. Morikoshi, Trans. Electr. Electron. Mater. 13 (2012) 171-176.
26. P.H. Haumesser, R. Gaumé, B. Viana, E. Antic-Fidancev, D. Vivien, J. Phys.: Cond. Matter 13 (2001) 5427-5447.
27. M. Ito, C. Goutaudier, Y. Guyot, K. Lebbou, T. Fukuda, G. Boulon, J. Phys.: Cond. Matter 16 (2004) 1501-1521.
28. B.F. Aull, H.P. Jenssen, IEEE J. Quantum Electron. 18 (1982) 925–930.
29. S.A. Payne, L.L. Chase, L.K. Smith, W.L. Kway, W.F. Krupke, IEEE J. Quantum Electron. 28 (1992) 2619–2630.
30. J.M. Serres, X. Mateos, P. Loiko, K. Yumashev, N. Kuleshov, V. Petrov, U. Griebner, M. Aguiló, F. Díaz, Opt. Lett. 39 (2014) 4247–4250.
31. P. Loiko, J.M. Serres, X. Mateos, H. Yu, H. Zhang, J. Liu, K. Yumashev, U. Griebner, V. Petrov, M. Aguiló, F. Díaz, IEEE Photonics J. 8 (2016) 1501312-1–12.
32. J. Liu, W. Han, X.n Chen, Q. Dai, H. Yu, H. Zhang, IEEE J. Sel. Top. Quantum Electron. 21 (2015) 1600808.
33. X. Chen, L. Wang, J. Liu, Y. Guo, W. Han, H. Xu, H. Yu, H. Zhang, Opt. Laser Technol. 79 (2016) 74-78.
34. H. Yuan, L. Wang, Y. Ma, X. Dou, W. Han, H. Xu, J. Liu, Z. Pan, Opt. Mater. Express 7 (2017) 3251-3260.

35. J. Liu, W. Han, X. Chen, D. Zhong, B. Teng, C. Wang, Y. Li, Opt. Lett. 39 (2014) 5881-5884.
36. L. Yang, B. Teng, D. Zhong, W. Han, J. He, Y. Xu, M. Zhu, J. Tang, S. Ji, J. Liu, Opt. Mater. Express 7 (2017) 3618-3625.
37. J. Liu, V. Petrov, H. Zhang, J. Wang, M. Jiang, Opt. Lett. 31 (2006) 3294-3296.
38. J.M. Serres, P. Loiko, X. Mateos, K. Yumashev, N. Kuleshov, V. Petrov, U. Griebner, M. Aguiló, F. Díaz, Opt. Mater. Express 5 (2015) 661-667.
39. L. Zhang, W. Chen, J. Lu, H. Lin, L. Li, G. Wang, G. Zhang, Z. Lin, Opt. Mater. Express 6 (2016) 1627-1634.
40. H. Chu, S. Zhao, K. Yang, J. Zhao, D. Li, G. Li, T. Li, W. Qiao, X. Xu, L. Zheng, J. Xu, Opt. Mater. 45 (2015) 181-184.
41. P. Loiko, J.M. Serres, X. Mateos, X. Xu, J. Xu, V. Jambunathan, P. Navratil, A. Lucianetti, T. Mocek, X. Zhang, U. Griebner, V. Petrov, M. Aguilo, F. Diaz, A. Major, Opt. Lett. 42 (2017) 2431-2434.
42. W. Han, X. Chen, L. Xia, S. Wang, H. Zhang, J. Liu, Opt. Express 22 (2014) 31404-31410.

Table 1. Structure data of a 3 at. % Yb^{3+}:CNGS crystal obtained after the Rietveld refinement.

Parameter	Notation, units	Value
Formula mass	g/mol	719.9226
Density (calculated)	ρ, g/cm^3	4.22
Space group		*P*321 (No. 150)
Point group		32
Number of formula units	Z	1
Lattice parameters	$a = b$, Å:	8.0890(2)
	c, Å:	4.9815(1)
	$\alpha = \beta$	90°
	γ	120°
Unit-cell volume	V, Å^3	282.30

Table 2. Atomic coordinates (x, y, z) for 3 at.% Yb^{3+}:CNGS obtained after the Rietveld refinement.

Site	Wyckoff	Occupancy	x	y	z
Ca	3*e*	0.97	0.419(2)	0	0
Yb	3*e*	0.03	0.419(2)	0	0
Nb	1*a*	1	0	0	0
Si	2*d*	1	1/3	2/3	0.557(5)
Ga	3*f*	1	0.742(1)	0	1/2
O1	2*d*	1	1/3	2/3	0.257(8)
O2	6*g*	1	0.495(6)	0.326(7)	0.300(9)
O3	6*g*	1	0.236(6)	0.099(5)	0.759(5)

Table 3. Selected interatomic distances for 3 at.% Yb^{3+}:CNGS obtained after Rietveld refinement.

Cation	Atom	Distance, Å	Cation	Atom	Distance, Å
Ca	O1×2	2.74(4)	Si	O1	1.49(9)
	O2×2	2.35(5)		O2×3	1.53(5)
	O2'×2	2.82(4)	$(Si-O)_{av}$		1.515
	O3×2	2.33(5)	Nb	O3×6	2.05(4)
$(Ca-O)_{av}$		2.563	$(Nb-O)_{av}$		2.05(4)
Ca	Ca×4	4.20(1)	Ga	O3×2	1.76(3)
	Ca'×2	4.9810(1)		O2×2	1.98(5)
$(Ca-Ca)_{av}$		4.591	$(Ga-O)_{av}$		1.826

Table 4. Output characteristics of CW 3 at.% Yb^{3+}:CNGS microchip lasers using 4-mm thick samples of different cut and a T_{OC} = 2.5% output coupler: λ_p – pump wavelength, w_p – pump spot radius in the focus, *Abs* – total pump absorption, P_{th} – laser threshold, P_{out} – maximum output power, λ_L – laser wavelength, η – slope efficiency vs. P_{abs}, η_{opt} – optical-to-optical efficiency vs. P_{inc}.

λ_p, nm	w_p, μm	Cut	*Abs*, %	P_{th}, W	P_{out}, W	λ_L, nm	η, %	η_{opt}, %
977-981	100	*a*-cut	22-43	1.36	3.28	1053	77	23
		c-cut	25-41	1.80	3.13	1051	83	23
976	52	*a*-cut	60	0.60	7.29	1048-1065	59	32
(VBG)		*c*-cut	58	0.55	7.61	1048-1060	59	33

Table 5. Output characteristics of some continuous-wave diode-pumped Yb^{3+}-doped lasers reported recently (* - this work).

Family	Crystal	Yb **doping**	**Cut**	P_{out}, W	η, %	λ_L, **nm**	Ref.
Borates	$YCa_4O(BO_3)_3$	15 at.%	Z-cut	8.35	70	~1040	[31]
		15 at.%	Y-cut	8.35	70	1039-1045	[32]
	$GdCa_4O(BO_3)_3$	10 at.%	Z-cut	18.2	70	1032	[33]
	$Sr_3La_2(BO_3)_4$	5 at.%	*a*-cut	8.2	33	~1040	[34]
Phosphates	$LuPO_4$	10 at.%	*a*-cut	1.61	75	1039	[35]
	YPO_4	5 at.%	*a*-cut	3.62	39	1014-1024	[36]
Vanadates	$LuVO_4$	1.5 at.%	*a*-cut	8.3	80	1031	[37]
Tungstates	$KLu(WO_4)_2$	3 at.%	N_g-cut	4.4	65	1049	[38]
	$MgWO_4$	1.25 at.%	X-cut	2.52	53	~1060	[39]
Silicates	$Ca_3NbGa_3Si_2O_{14}$	3 at.%	*c*-cut	7.61	59	1048-1060	*
	$(Gd_{0.1}Y_{0.9})_2SiO_5$	5 at.%	*a*-cut	~1	18	1060, 1080	[40]
Aluminates	$CaAlGdO_4$	8 at.%	*a*-cut	7.79	84	1057-1065	[41]
	$CaAlYO_4$	3 at.%	*a*-cut	5.06	91	1048-1056	[41]
Garnets	$Y_3Sc_2Ga_3O_{12}$	5 at.%	-	7.9	60	1038-1041	[42]

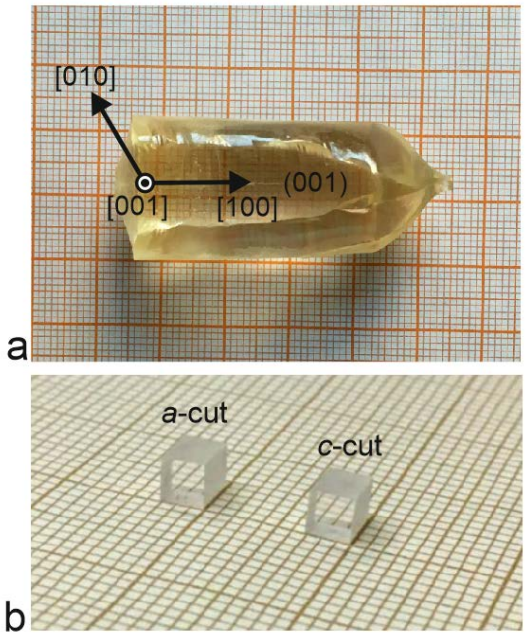

Figure 1. (a) As-grown boule of a 3 at.% Yb^{3+}:CNGS crystal (growth along the [100] direction); the labels denote the principal crystallographic directions and the (001) natural face; (b) photographs of the *a*-cut and *c*-cut laser-grade polished 4 mm-thick crystal samples.

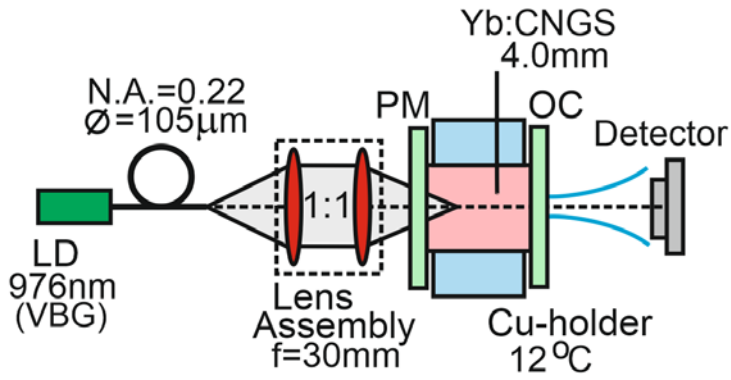

Figure 2. Scheme of the microchip laser set-up: LD – laser diode, PM – pump mirror, OC – output coupler.

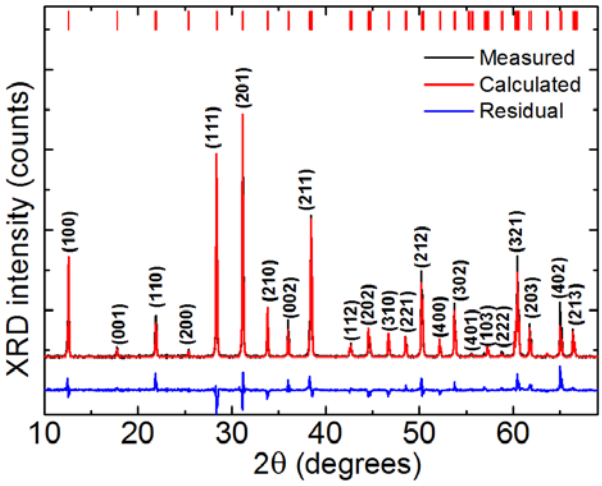

Figure 3. Measured (black), calculated (red), and differential (blue) X-ray diffraction, XRD patterns for a 3 at.% Yb^{3+}:CNGS crystal powder obtained after the Rietveld refinement (at room temperature). The labels with the (hkl) Miller's indices correspond to the Bragg reflections.

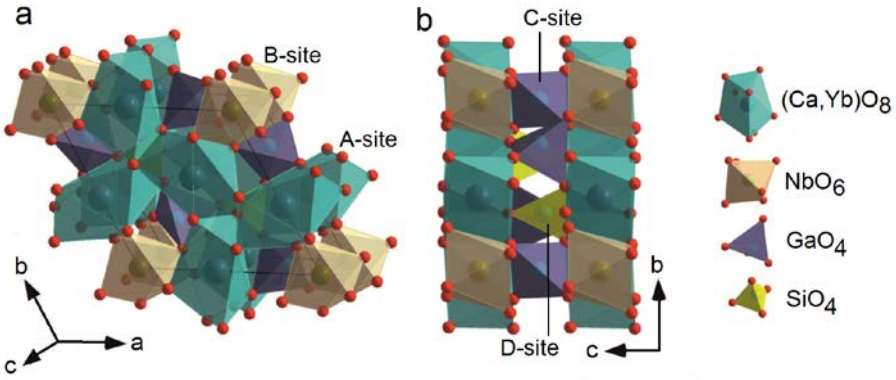

Figure 4. (a,b) Fragment of the Yb^{3+}:CNGS structure projected on the *a-b* and *b-c* planes (according to the data from the Rietveld refinement).

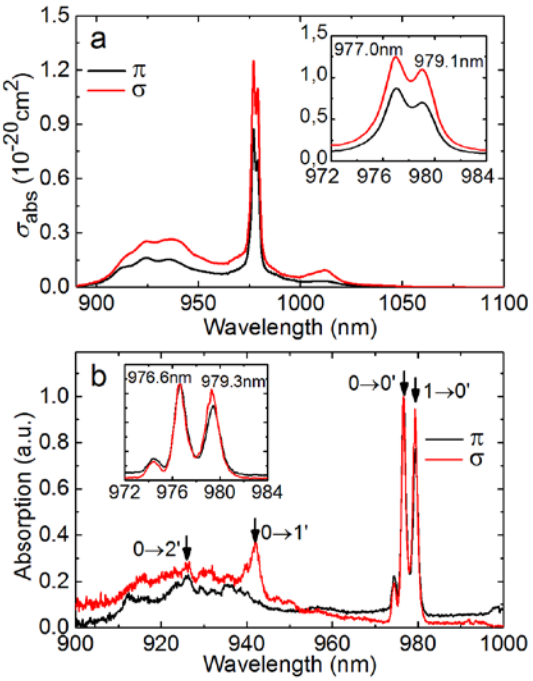

Figure 5. Absorption spectra of a 3 at.% Yb^{3+}:CNGS crystal for light polarizations π and σ measured at (a) RT (293 K) and (b) at LT (6 K), *insets* in (a) and (b) show the structure of the absorption peak around the ZPL. The arrows and the corresponding labels in (b) indicate the observed transitions between the Stark sub-levels, $i \rightarrow j'$.

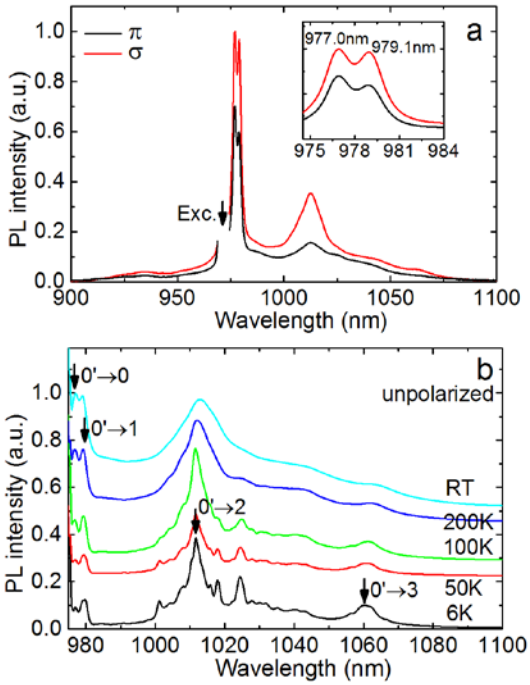

Figure 6. Photoluminescence (PL) spectra of a 3 at.% Yb^{3+}:CNGS crystal: (a) emission spectra measured at RT (293 K) for light polarizations π and σ, *inset* shows the structure of the emission band around the ZPL; (b) unpolarized emission spectra from 6 to 293 K, λ_{exc} = 972 nm. The arrows and the corresponding labels in (b) indicate the observed transitions between the Stark sub-levels, $j' \rightarrow i$.

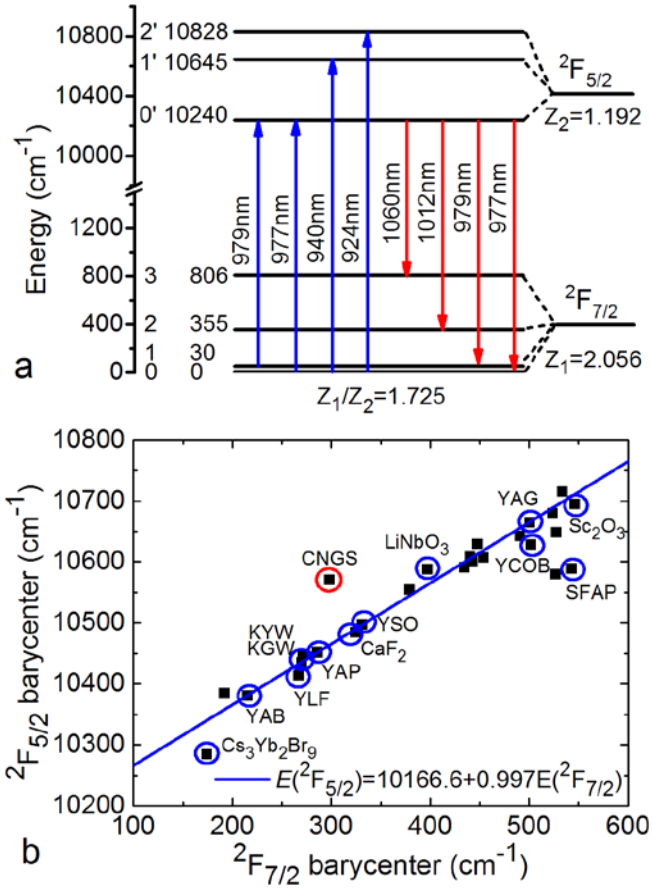

Figure 7. (a) Scheme of the Stark sub-levels of the Yb^{3+} ion in CNGS; the *arrows* denote the observed transitions at 6 K. $Z_1(Z_2)$ are the partition functions for the lower(upper) multiplets; (b) barycenter plot for various Yb^{3+}-doped crystals.

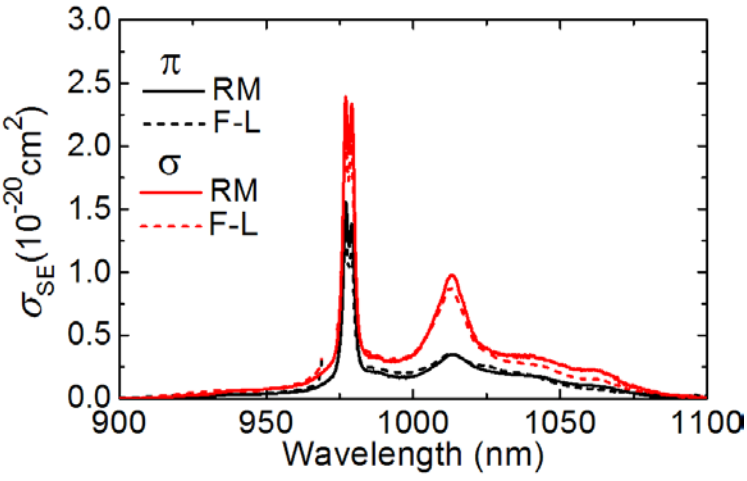

Figure 8. Polarized stimulated-emission cross-section, σ_{SE}, spectra for Yb^{3+}-doped CNGS at RT, calculated with the reciprocity method (RM) and Füchtbauer–Ladenburg (F-L) formula. The light polarizations are π and σ.

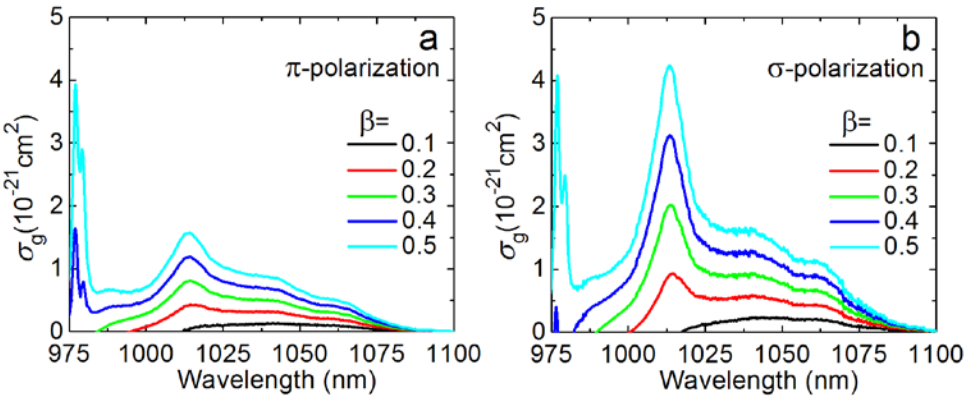

Figure 9. Polarized gain cross-section, $\sigma_g = \beta\sigma_{SE} - (1-\beta)\sigma_{abs}$, spectra for Yb^{3+}-doped CNGS at RT. The light polarizations are π (a) and σ (b), $\beta = N_2(^2F_{5/2})/N_{Yb}$ is the inversion ratio. The spectra are calculated using the σ_{SE} values obtained with the reciprocity method.

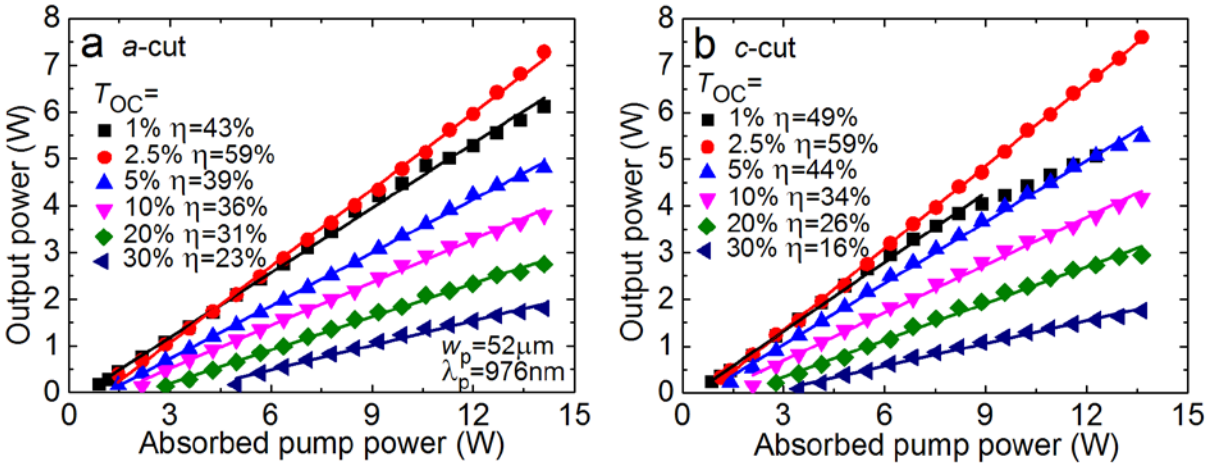

Figure 10. Input-output dependences for the CW diode-pumped 3 at.% Yb^{3+}:CNGS microchip lasers based on (a) *a*-cut or (b) *c*-cut crystals. The pump is a VBG-stabilized diode laser at 976 nm. Pump spot radius: w_p = 52 μm, crystal thickness: 4 mm, η – slope efficiency.

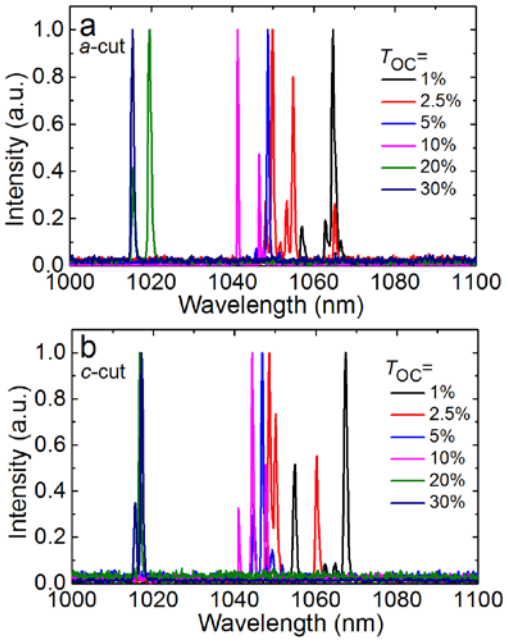

Figure 11. Typical emission spectra for the CW 3 at.% Yb^{3+}:CNGS microchip lasers based on (a) *a*-cut or (b) *c*-cut crystals for various transmissions of the output coupler T_{OC}. The pump is a VBG-stabilized diode laser at 976 nm and the pump spot radius is w_p = 52 μm. The spectra are measured at the maximum P_{abs} (cf. Fig. 10).